Heliyon 10 (2024) e35769

Contents lists available at ScienceDirect

Heliyon

journal homepage: www.cell.com/heliyon

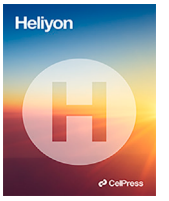

Research article

3D physiologically-informed deep learning for drug discovery of a novel vascular endothelial growth factor receptor-2 (VEGFR2)

Mengyang Xu [a], Xiaoyue Xiao [a], Yinglu Chen [a], Xiaoyan Zhou [a], Luca Parisi [b], Renfei Ma [a,*]

[a] Faculty of Biology, Shenzhen MSU-BIT University, Shenzhen, 518172, Guangdong, China
[b] Department of Computer Science, Tutorantis, Edinburgh, EH2 4AN, Scotland, United Kingdom

ARTICLE INFO

Keywords:
VEGFR2
Drug discovery
Structural modeling
Deep learning
Geometric deep learning

ABSTRACT

Angiogenesis is an essential process in tumorigenesis, tumor invasion, and metastasis, and is an intriguing pathway for drug discovery. Targeting vascular endothelial growth factor receptor 2 (VEGFR2) to inhibit tumor angiogenic pathways has been widely explored and adopted in clinical practice. However, most drugs, such as the Food and Drug Administration –approved drug axitinib (ATC code: L01EK01), have considerable side effects and limited tolerability. Therefore, there is an urgent need for the development of novel VEGFR2 inhibitors. In this study, we propose a novel strategy to design potential candidates targeting VEGFR2 using three-dimensional (3D) deep learning and structural modeling methods. A geometric-enhanced molecular representation learning method (GEM) model employing a graph neural network (GNN) as its underlying predictive algorithm was used to predict the activity of the candidates. In the structural modeling method, flexible docking was performed to screen data with high affinity and explore the mechanism of the inhibitors. Small -molecule compounds with consistently improved properties were identified based on the intersection of the scores obtained from both methods. Candidates identified using the GEM-GNN model were selected for in silico modeling using molecular dynamics simulations to further validate their efficacy. The GEM-GNN model enabled the identification of candidate compounds with potentially more favorable properties than the existing drug, axitinib, while achieving higher efficacy.

1. Introduction

Cancer remains a significant global health concern, with nearly 10 million deaths (approximately one in six) reported by the World Health Organization [1,2]. Tumor cells take advantage of their microenvironment by releasing growth factors and cytokines that can activate surrounding normal quiescent cells and initiate a cascade of rapidly dysregulated events [3]. Once the tumor lesion exceeds a few millimeters in diameter, hypoxia and nutrient deprivation induce an “angiogenic switch” that facilitates tumor progression [4]. Therefore, modulation of the angiogenic process is recognized as an important approach for cancer treatment [5,6].

The vascular endothelial growth factor (VEGF)-vascular endothelial growth factor receptor (VEGFR) pathway is a fundamental mechanism influencing various stages of angiogenesis, including vascular permeability, endothelial cell survival, proliferation, migration, invasion into the neighboring tissue, and capillary-like tube formation [7,8]. A critical step in angiogenesis involves the

* Corresponding author.
E-mail address: marenfei@smbu.edu.cn (R. Ma).

https://doi.org/10.1016/j.heliyon.2024.e35769
Received 11 June 2024; Received in revised form 1 August 2024; Accepted 2 August 2024

Available online 8 August 2024

upregulation of pro-angiogenic growth factor receptors on endothelial cells, with VEGFR2 emerging as the most important factor in promoting angiogenesis. VEGFR2, which is a transmembrane tyrosine kinase receptor, undergoes abnormal activation or overexpression during cancer development [9,10]. By inhibiting the tyrosine kinase signaling pathway of VEGFR2, it is possible to disrupt and prevent angiogenesis during tumor proliferation [11]. Recently, VEGFR inhibitors have been extensively investigated as potential treatment options for metastasis. Several inhibitors, including axitinib, pazopanib, sorafenib, sunitinib, and tizanib, along with other drugs, have been shown to be effective against a variety of cancers, including breast, colorectal, and lung cancers [12–14]. Axitinib, a small molecule targeting VEGFR2, has demonstrated antitumor activity against various types of cancer cells, including those resistant to conventional chemotherapy and targeted therapies. Clinical trials have revealed that axitinib significantly enhances overall and progression-free survival in patients with advanced renal cell carcinoma and hepatocellular carcinoma [15]. However, similar to most current tyrosine kinase inhibitors, axitinib has considerable side effects, such as the development of resistance mechanisms [16], off-target effects [17], and gastrointestinal toxicity [18,19].

The existing constraints associated with small- molecule inhibitors of VEGFR2 and the complexities inherent in their development underscore the necessity for innovative compounds capable of effectively targeting this key protein [20]. As computational resources and algorithmic techniques continue to progress, the integration of computational approaches into drug discovery has emerged as a promising tool to address this challenge, because virtual screening allows the rapid identification of potential lead compounds without the need for resource-intensive experimental screening [21]. As a result, computational methods allow researchers to assess the developability of drug candidates in the early stages, thereby facilitating the optimization of lead compounds and the development of safer and more efficacious drugs [22,23].

In general, the computational methodologies employed in drug discovery can be broadly categorized into two groups: data-driven approaches, which leverage big data, and data-driven techniques (e.g., artificial intelligence, deep learning, and machine learning) [24–27], and physics-based multiscale modeling methods [28], as demonstrated by tools such as Rosetta [24], molecular dynamics (MD) simulation [29,30], and molecular docking [31]. Within data-driven methods, particularly artificial-intelligence-driven drug discovery (AIDD), many machine learning algorithms are employed to analyze the vast amounts of data generated during the drug discovery process. These algorithms are effective at distinguishing intricate patterns and relationships that are challenging or not feasible for manual identification. For instance, AIDD uses machine learning algorithms to scrutinize databases containing chemical and biological information such as gene expression data, protein structures, and compound libraries [32]. This analytical approach facilitates the identification of potential drug targets and streamlines the initial stages of drug discovery. The AIDD algorithm is proficient in predicting the physical and chemical properties of molecules, including solubility, log P, and pKa values. This predictive capability helps in the optimization of lead compounds and the avoidance of synthesizing impractical candidates, identifying those with the most promising therapeutic potential. The other type is the physics-based multiscale modeling method, which can be termed structure-based drug design (SBDD) because it relies on structural information pertaining to drugs and their targets. SBDD employs computational methods to forecast the binding affinity between small molecules and protein targets, as well as other properties, such as stability. This approach enables the design of drugs that interact specifically with certain proteins, modulate their specificity to address the underlying disease mechanism, and reveal their developability [33].

Given the limitations associated with small-molecule inhibitors of VEGFR2, in this study, we propose a novel strategy for efficiently designing potential candidates targeting VEGFR2 using three-dimensional (3D) deep learning and structural modeling. A geometrically enhanced molecular representation learning method (GEM) model with a graph neural network (GNN) was employed as the underlying algorithm to predict the pharmacological activities of the candidates. For structural modeling, flexible docking was conducted to screen candidates with high affinity and to explore the efficacy pathways and safety profiles of the inhibitors. Small-molecule compounds exhibiting consistently superior efficacy were identified based on the intersection of scores derived from both methods. Candidates selected using these two approaches were used to perform MD simulations to further validate their properties and efficacy.

2. Methods

2.1. Schematic of the proposed method

This study employed an integrated approach combining AIDD and SBDD to systematically screen and identify small-molecule drugs with specific targeting capabilities towards VEGFR2, as illustrated in Fig. 1. Initially, 11,521 compounds with documented biological activities and structural features were extracted from the BindingDB database. The construction of the GEM model, based on the GNN, served as the foundation for the VEGFR2 activity prediction algorithm used in this study to predict the activity of compounds within the database [34]. Next, the binding affinity of the candidate small-molecule compounds to VEGFR2 was evaluated using flexible docking. Candidates were then selected based on the combined outcomes of the GEM model and flexible docking results. Finally, the structures of the chosen candidates in complex with VEGFR2 were analyzed using MD. These candidates represent potential breakthroughs in cancer treatment. In the literature, axitinib was employed as a standard reference drug to assess the anti-tumor effects of prospective new drug candidates aimed at inhibiting VEGFR2 in numerous studies [35,36]. Consistent with established studies, axitinib was also adopted as a control compound to assess the viability of these candidates identified in this study.

2.2. Dataset preparation

In this study, the BindingDB and ChEMBL21 databases were selected for their extensive and meticulously curated datasets, providing abundant bioactivity data relevant to VEGFR2. BindingDB, a well-established repository specializing in the binding affinities

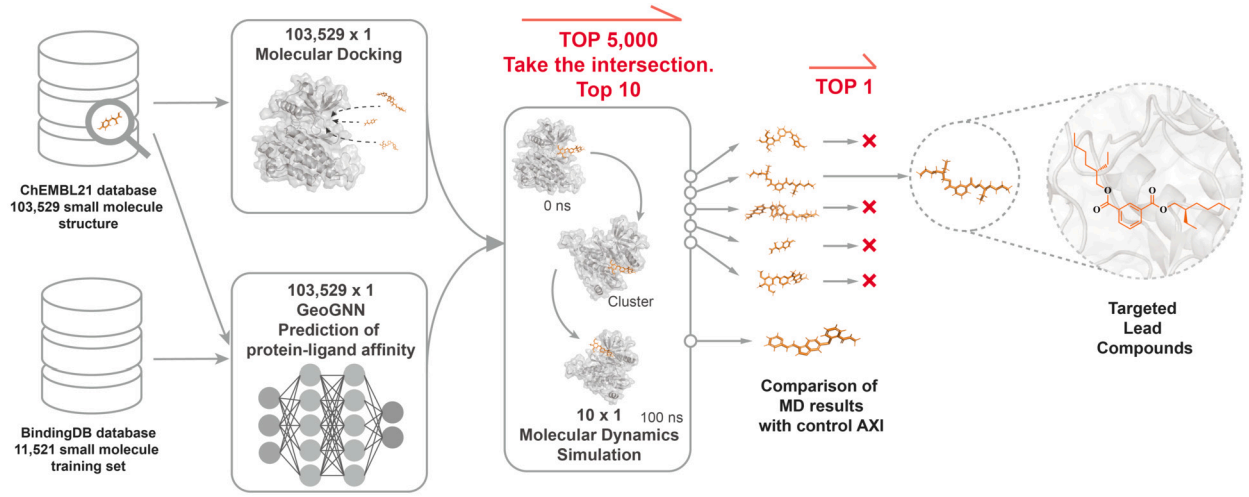

Fig. 1. A flowchart of the overall screening strategy.

of small molecules, was chosen for investigating drug-target interactions [37]. This database encompasses over 14,607 unique small molecule structures targeting VEGFR2, from which a subset of 11,521 small molecules with Ki (nM) values greater than zero were identified for further analysis.

Additionally, a comprehensive docking dataset from the ChEMBL21 database [38] was obtained, including 103,529 small molecule structures represented by both isomeric and canonical simplified molecular input line entry system (SMILES) (iso-SMILES and canonical SMILES). ChEMBL21 is well-known for its extensive collection of bioactive molecules, including numerous FDA-approved drugs. This database is specifically tailored for drug discovery research, providing high-quality data that enhances the reliability of computational analyses.

These databases were preferred over alternatives such as DrugBank [39] or PubChem [40] due to their emphasis on bioactivity and binding affinity data, crucial for computational approach developed in this study. The curated nature of BindingDB and ChEMBL21 ensures data reliability and relevance, significantly enhancing the data robustness of this study.

2.3. Structure preparation

The crystal structure of the human VEGFR2 kinase domain (PDB: 1VR2) was obtained from the Protein Data Bank [41]. The structure was prepared, protonated in 3D, and subjected to energy minimization using the Molecular Operating Environment (MOE) software. Due to its comprehensive suite of tools and demonstrated accuracy in docking studies, MOE has been widely utilized and validated in the literature [27,42]. MOE has been shown to achieve comparable results to other popular software packages such as Schrödinger and Autodock Vina. For instance, both MOE and Schrödinger's Covalent Dock programs successfully predicted binding affinities in [42]. Therefore, MOE was chosen for this study to maintain consistency. The structure preparation involved the correction of gaps in the protein structure. Protonation in 3D includes the addition of hydrogen atoms, while considering the default ionization states. Flip options were applied to optimize the hydrogen-bonding networks involving amide, sulfonamide, and imidazole groups. All the water molecules were removed from the structure. The atom constraint strength was set to 10, and a flat-bottom constraint range of 0.25 was applied to prevent excessive positional deviation of the atoms. The protein conformation was optimized through energy minimization using the root mean square gradient (RMSG) method with a convergence threshold of 0.1 kcal/mol/Å.

2.4. AIDD

2.4.1. The graph-based molecular representations

The use of graph models to represent molecular information offers several advantages. In contrast to text-based representations of molecular data, such as SMILES and InChI (International Chemical Identifier), graph models offer a more intuitive representation of molecular structures using nodes and edges to represent atoms and their bonds. Consequently, the chemical information of a molecule can be captured more accurately [34,43]. In this study, the molecular representation comprised two distinct graphs, namely, the bond-angle graph denoted as H and the atom-bond graph denoted as G. Graph G describes the correlation between atoms and chemical bonds, representing atoms as nodes and chemical bonds as edges connecting these nodes. In the bond-angle graph, the nodes represent chemical bonds, whereas the bond angles are regarded as graph edges. Each bond angle links two and three chemical bonds, resulting in a three-dimensional conformation of the molecule. Notably, unlike graph G, graph H captures the spatial arrangement of the molecular structure [44]. Both the atom-bond graph and bond-angle graph served as inputs to the geometry-based graph neural network (GeoGNN), contributing to a comprehensive analysis and understanding of molecular information within the context of graph neural networks [34]. More details for GeoGNN can be found in [34].

2.4.2. Training settings and parameters

During the training process, a batch size of 256 was employed, the number of training epochs was 800, and validation evaluation metrics were adapted for early stopping. Adam was used as the optimizer with a weight decay of 0.0008. The cosine-annealing learning rate was employed for the schedule of the learning rates, with a specific learning rate of 0.001 and the maximum number of iterations (Tmax) set to 15. To predict the molecular properties, the dataset obtained from the BindingDB database was randomly split in an 8:2 ratio to derive the training and testing datasets. The ReLU activation function was applied, and the loss functions were the root mean squared error (MSE), mean absolute error (MAE), and coefficient of determination (R2). Additionally, layer normalization, regularization, and graph normalization were considered in GeoGNN to enhance the predictive performance [45]. All experiments were conducted on a computing system equipped with an NVIDIA GeForce RTX 3090 GPU and a 256-core AMD EPYC 7742 CPU.

2.5. Molecule docking

Molecular docking experiments were performed using MOE software, employing a dataset of 103,529 FDA-approved small-molecule drugs. The structure of the kinase domain (PDB: 1VR2) of human VEGFR2 (KDR) was retrieved from the Protein Data Bank for the docking study [41]. After structure retrieval, structure preparation, 3D protonation, and energy minimization procedures were performed using MOE. Specifically, the structure preparation phase repaired gaps in the protein structure, whereas 3D protonation added hydrogen atoms to the structure and completed protonation in the default ionization state. Water molecules were removed systematically. The atomic restraint strength was set to 10, and the extent of the flat-bottom restraint was set to 0.25 to prevent excessive positional deviations of atoms. Energy minimization was performed with a root mean square gradient of 0.1 kcal/mol/Å to optimize the protein conformation. The binding site for VEGFR2 was identified based on complexes of existing small-molecular inhibitors, and VEGFR2 (PDB: 1Y6A, 1YWN, 3CPC, 4AG8, 3WZE).

Molecular docking was performed using the method specifically designed for high-throughput docking, as shown in Eq. (1). The docking outcomes were ordered based on the dock score, which is a scoring metric primarily contingent on the interaction energy between ligands and the VEGFR2 protein. Additionally, the binding free energy of the docking outcomes underwent assessment through the generalized Born/volume integral/weighted surface area (GBVI/WSA) dG scoring method, introduced by Corbeil et al. [46], as follows:

$$\Delta G \approx c + \alpha \left[\frac{2}{3} (\Delta E_{Coul} + \Delta E_{sol}) + \Delta E_{vdW} + \beta \Delta SA_{weighted} \right] \tag{1}$$

This method incorporates various terms, including the average gain and loss of rotation and translation entropy (c), a constant ($\alpha.\beta$) determined during the function training process, a Coulomb electrostatic term (ECoul), a solvation electrostatic term calculated using the GB/VI solvation model (Esol), a van der Waals contribution (EvdW), and the surface area weighted according to the exposed area (SAweighted).

2.6. Molecular dynamics simulations

MD simulations were conducted using GROMACS 2020.05 software [47]. The SwissParam server was used to generate topology files for the ligands [48]. The system was prepared by placing protein-ligand complex structures in periodic cubic boxes with a boundary size of 1.2 nm. NaCl was added at a concentration of 0.15 mol/L for charge neutralization. An energy minimization procedure was performed using a maximum descent algorithm, with up to 5,000 steps employed to optimize the system structure. Pre-equilibration phases, including 1 ns of a constant number of particles, volume, and temperature (NVT) and 1 ns of a constant number of particles, pressure, and temperature (NPT) were performed. The system temperature was maintained at 310 K, and the pressure was set to 1 bar using the V-rescale [49] and Parrinello-Rahman algorithms [50]. The formal simulation duration was 100 ns, with a time step of 2 fs. The CHARMM36 force field was applied to all simulations [51].

Following the simulations, the stability of protein-small molecule drug binding was assessed by analyzing the RMSD of the interactions within the simulation trajectories. The truncation distances for van der Waals and Coulomb interactions were set to 1 nm. GROMACS was employed for trajectory analysis, including structural clustering, based on the RMSD of the atomic coordinates. Clusters were identified by comparing the mean RMSD of the largest cluster with those of other structures. Mean square displacement (MSD) calculations reflect the diffusion constants of molecules, offering insights into conformational changes in protein complexes and their functional implications. The binding stability of the complex was evaluated by calculating the root mean square fluctuation (RMSF), which reflects the magnitude of the fluctuation of the protein complex around its equilibrium position. Solvent-accessible surface areas (SASAs) provide information about the different regions of a molecule exposed to the solvent environment, aiding the understanding of small molecules or proteins binding to specific sites on the protein surface and their impact on protein function [52]. Energy calculations provide insights into the stability of the complex and how it is influenced by various factors, such as temperature, pressure, or the presence of ligands.

3. Results

3.1. Prediction of protein-ligand affinity

The prediction of protein-ligand affinity is of vital significance in the field of computational drug design. Prior to the training phase, the Morgan fingerprint was computed using RDKit and the high-dimensional Morgan fingerprint data underwent dimensionality

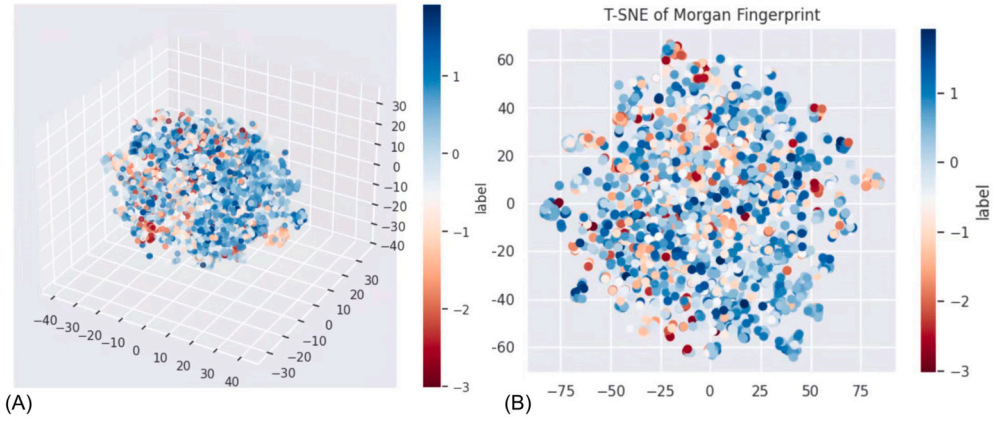

Fig. 2. The distribution of molecules is illustrated in both the three-dimensional space (A) and two-dimensional space (B). The dataset underwent an 80/20 split for training and validation purposes. T-SNE, t-distributed stochastic neighbor embedding.

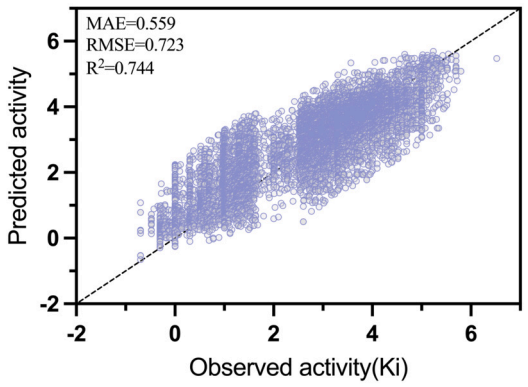

Fig. 3. The predictive performance of the geometry-based graph neural network in estimating Ki values as compared to the observed Ki values sourced from DrugBank. The dashed line represents the identity line (y = x). Evaluation metrics encompassing R^2, mean absolute error (MAE), and root mean squared error (RMSE) values served as the indicators of the accuracy and predictive efficacy of the model.

reduction through t-distributed stochastic neighbor embedding. This reduction facilitates the visualization and analysis of molecular distributions in both 3D and 2D spaces. Potential outlier molecules were identified by measuring the distances from each data point to the centroid in the 3D space. Outliers were defined as data points with distances exceeding three times the standard deviation of the mean distance. The identified outliers were removed from the dataset to improve data quality.

The distributions of molecules in both 3D and 2D spaces are illustrated in Fig. 2. The data points are color-coded based on the labels for informative representation. The molecular dataset exhibited strong clustering behavior, indicating that the extracted molecular features and dimensionality reduction techniques employed effectively captured the underlying structure within the dataset. This data processing procedure is expected to be advantageous for subsequent training processes.

The predicted results, R^2, mean absolute error (MAE), and root mean square error (RMSE) are shown in Fig. 3. It can be seen that the predicted results and observed results were highly correlated, which indicates that the GeoGNN had a good predictive capability since the R2 and RMSE were larger than 0.7 ($p - value < 0.001$ for R^2, indicating a highly statistically significant correlation) and the MAE was below 0.6. Therefore, the model used in this study can learn the molecular structure-affinity relationship well.

3.2. Molecular docking

Docking tests were performed using the 103,529 small molecules. The GBVI scoring function [53] was employed to estimate the free energy associated with ligand binding, considering a specified molecular posture. This scoring function served as a metric for evaluating the docking posture. Successful docking and scoring were achieved for 88,785 small molecules, resulting in the identification of the top 5,000 compounds. The intersection of the prediction score Ki and the docking result score S of the top 5,000 compounds in the AI model and the 10 screened compounds, as detailed in Supplementary Table S1, with better composite scores are shown in Figs. 4 and 5, respectively. Although these compounds are structurally diverse, it is important to note that the nature of protein-ligand interactions and the intrinsic properties of the binding pockets enable structurally diverse molecules to selectively bind to specific pockets, as demonstrated by studies in the literature [54–56].

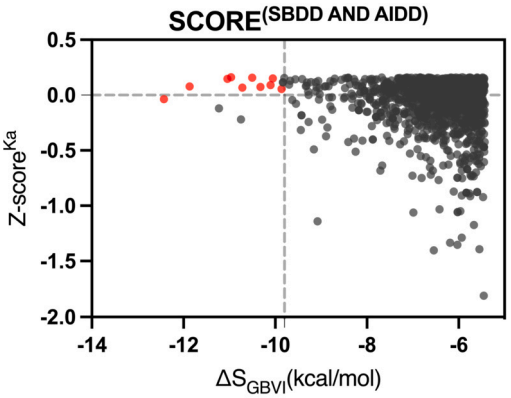

Fig. 4. The intersection of the top 5,000 compounds based on the AI model prediction score (Ki) and the docking result score (S) is depicted. The red dots represent data points corresponding to the 10 compounds exhibiting superior composite scores.

Table 1
Predicted oral rat LD_{50} for the 10 compounds screened and the positive control compound axitinib from the nearest neighbor method.

Compounds	Oral rat LD_{50} -Log10 (mol/kg)	Oral rat LD_{50} mg/kg
1	2.58	1582.17
2	4.02	72.40
3	1.70	11991.17
4	3.14	290.89
5	1.42	18778.73
6	1.42	18778.73
7	2.85	874.82
8	2.03	4230.54
10	2.77	1084.92
11	1.12	29337.37
axitinib	**2.45**	**1373.50**

Given that toxicity assessment is a critical part of the drug discovery process, the United States Environmental Protection Agency (EPA)'s Toxicity Estimation Software Tool (TEST) [57], which was widely employed in the literature for toxicity analysis [58–60], was employed to estimate the toxicity of the 10 compounds screened and the positive control compound axitinib. During the estimation process, the nearest neighbor method was used to estimate the oral rat LD_{50}, which is the lethal dose for half of a group of 10 or more laboratory white rats when administered orally as a single dose. The results are shown in Table 1.

3.3. MD

AIDD focused on assessing the binding affinity of small-molecule compounds to VEGFR2, whereas docking experiments concentrated on evaluating the stability of the docking poses assumed by these compounds in relation to VEGFR2. A combination of results from both methods was used to select small-molecule compounds for subsequent MD simulations. Specifically, the top 5% (5,000) of intersections derived from the outcomes of the AIDD and docking analyses were selected. Notably, 100-ns MD simulations were performed for the top 10 small-molecule compounds within this intersection set, alongside the positive control axitinib.

Examination of the structures at 100 ns revealed that no small-molecule compounds detached from the binding pocket. The long chains of the small-molecule compounds showed robust and stable binding within the pocket (Supplementary Figure MD_frame). Compounds 1, 2, and 10 were partially exposed to the solvent environment and were unable to maintain a stable binding conformation, as depicted in A, B and I in the Supplementary Figure MD_frame. In contrast, compounds 3, 4, 6, 7, 8, and 11 at 100 ns and their intermediate (cluster) structures were essentially the same, suggesting their capacity for more secure binding to VEGFR2 (see C, D, F, G, H, and J in the Supplementary Figure MD_frame). Consequently, the six small-molecule compounds, along with the control, underwent further detailed analysis.

The results of the 11 compounds as representative examples of the MD analysis are shown in Fig. 6. The RMSD, a metric for gauging the average positional alteration of all atoms between two structures, was employed in the analysis. The RMSD calculations based on the initial structure revealed a notable phase of increased values at approximately 5 ns for all ligands. However, except for compounds 3, 8, and 10, the ligands converged to stable states in the middle of this period. Specifically, compounds 4, 7, 11, and the control compound exhibited relatively constant RMSD values throughout the simulation process. A comparison of the RMSD values among the 11 simulated complexes revealed that the control compound, compound 11, and compound 2 exhibited smaller values and a stabilizing trend. Notably, when the RMSD of compound 11 stabilized, its value was the smallest among the 10 compounds, suggesting minimal postural changes during the simulation (see J in Supplementary Figure RMSD).

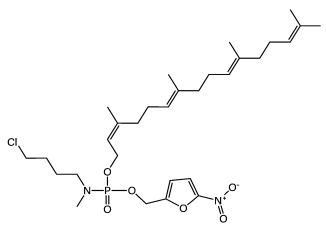

Compound 1
GGTI-2Z
(5-Nitro-2-furanyl) methyl ((2Z,6E,10E)-
3,7,11,15-tetramethyl-2,6,10,14-hexadecatetraen-1-yl)
N-(4-chlorobutyl)-N-methylphosphoramidate

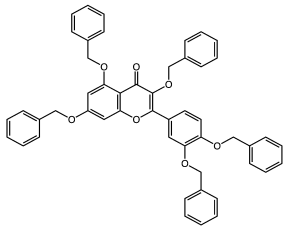

Compound 2
Benzquercin
2-[3,4-bis(pheny|methoxy)phenyl]-
3,5,7-tris(phenylmethoxy)chromen-4-one

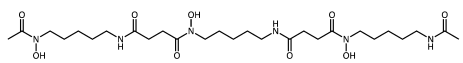

Compound 3
Desferrioxamine D1
N'-[5-[[4-[5-acetamidopentyl(hydroxy)amino]-4-
oxobutanoyljamino]pentyl]
-N-[5-[acetyl(hydroxy)amino|pentylj-N'-hydroxybutanediamide

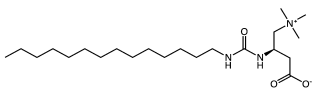

Compound 4
Teglicar
(3R)-3-(tetradecylcarbamoylamino) -4- (trimethylazaniumyl)butanoate

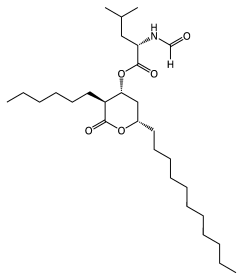

Compound 5
N-Formyl-L-leucine(3S,4R,6S)-
3-hexyl-2-oxo-6-
undecyltetrahydro-2H-pyran-4-yl ester

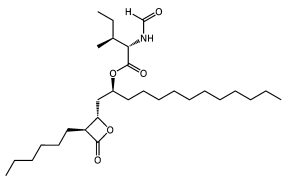

Compound 6
L-Isoleucine Orlistat
((2S)-1-[(2S,3S)-3-hexyl-4-oxooxetan
-2-yl|tridecan-2-yl] (2S,3S)-2-
formamido-3-methylpentanoate

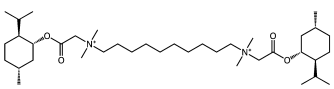

Compound 7
Decamethoxin ion
10-(dimethyl-[2-((1R,2S,5R)-5-methyl-2-propan-
2-ylcyclohexyl|oxy-2-oxoethyl|azaniumyl
[decy/-dimethyl-[2-[(1R,2S,5R)-5-methyl
-2-propan-2-ylcyclohexyljoxy-2-oxoethyljazanium

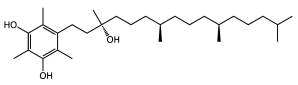

Compound 8
alpha-Tocopherylhydroquinone
2-|(3R,7R, 11R)-3-hydroxy-3,7,
11,15-tetramethylhexadecyl-3,5,6-
trimethylbenzene-1,4-diol

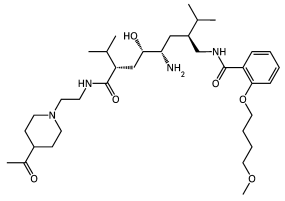

Compound 10
CGP-62198A monohydrochloride
N-((2S,4S,5S,7S)-7-|2-(4-acety|piperidin-1-yl)ethylcarbamoyl]
-4-amino-5-hydroxy-8-methyl-2-propan-2-yinonyl)-2-
(4-methoyvbutoxy)benzamide:hvdrochlorider

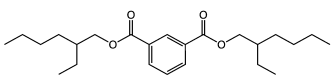

Compound 11
Bis(2-ethylhexyl) isophthalate
bis (2-ethwihexvi) benzene- 1.3-dicarboxylate

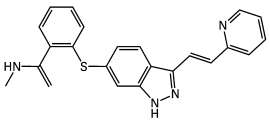

Compound Control
AXT(Axitinib)
N-methyl-2-((3-((E)-2-pyridin-2-ylethenyl]
-1H-indazol-6-yl[sulfanyl|benzamide

Fig. 5. The 10 compounds screened and the positive control compound axitinib.

The MD results for the best-performing compound, compound 11, and the MD data for the control drug, axitinib, are shown in Fig. 7. Notably, RMSD analysis revealed that compound 11 displayed greater stability than axitinib after 80 ns, with a reduction in relative atom displacement. MSD analysis revealed that compound 11 exhibited significant protein and ligand positional changes at 50 ns. Importantly, at 50 ns post-stabilization, the trend and magnitude of the positional changes in compound 11 aligned with those observed for axitinib.

4. Discussion

MD analysis revealed a notable observation that the control ligand exhibited a change in RMSD during the later stages of the simulation. This finding suggests a potential ongoing alteration in the binding conformation of the control ligand, while compound 11 remained more stable. The MSD was employed to scrutinize the positional alterations in the proteins and ligands. Prior to 80 ns,

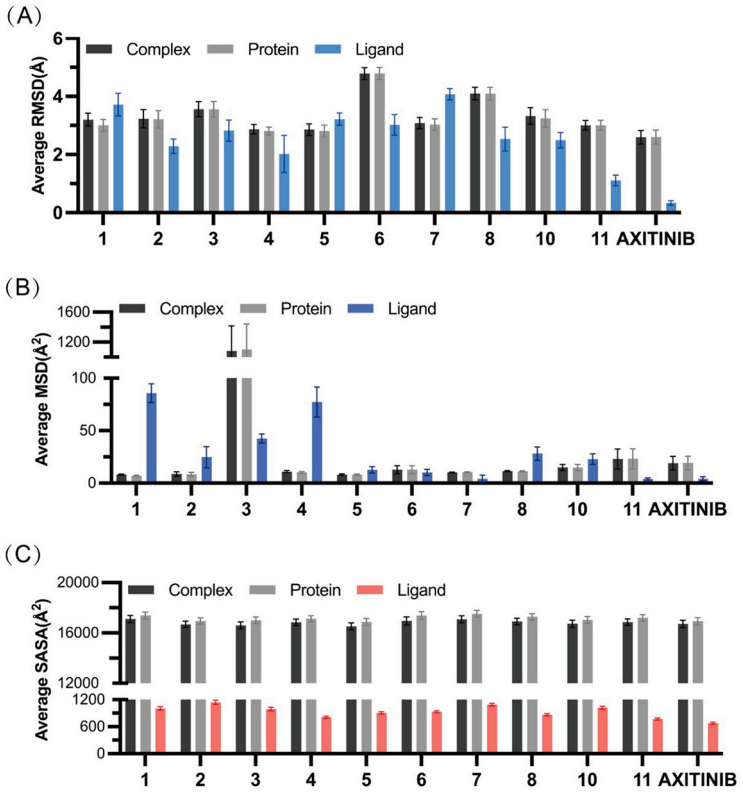

Fig. 6. Mean and standard deviation of the root mean square deviation (RMSD) (A), mean square displacement (MSD) (B), and solvent-accessible surface area (SASA) (C) for 10 representative compounds and the control compound axitinib at 50 ns post-stabilization after the simulation.

the MSD values for both the control compound and compound 7 remained notably stable. Notably, compounds 3, 6, and 11, and the control compound displayed similar trends in MSD values for the proteins and ligands, whereas other compounds demonstrated considerable variation in MSD values (see Supplementary Figure MSD). Such discrepancies may contribute to larger relative displacements between the proteins and ligands, leading to diminished stability. Gyrate, is a metric reflecting molecular volume and shape, with an increased value indicating an expanded system. Specifically, the gyrations of compounds 2, 5, 6, 7, and 11 and the control compound demonstrated greater stability than the other two molecules (see Supplementary Figure gyrate_ligand). Moreover, the linear structures of compounds 2, 5, 7, and 11 and the control compound were evidenced by lower X-axis components, with gyrations primarily stemming from the planes where the Y- and Z-axes reside. Conversely, the gyrations of compounds 3, 4, and 8 exhibited sustained variability throughout the simulation, maintaining alterations in the three-axis components within a varied range (see Supplementary Figure gyrate_ligand). Compound 11 and the control compound showed similar changes in the three-axis components, with changes in the X-axis maintained at relatively larger intervals. Eleven compounds, excluding compound 3, exhibited a stable trend in gyration throughout the simulation (see Supplementary Figure gyrate_protein). Notably, compounds 6, 7, 8, and 10 exhibited a volumetric change at approximately 40 ns and stabilized thereafter, suggesting a ligand-driven conformational adjustment towards increased affinity.

The RMSF reflects the average positional change amplitude of the residual atoms in 100 ns. The distribution of the RMSF among the protein residues across all 11 compounds exhibited a similar pattern, as illustrated in Supplementary Figure RMSF. Compound 3 showed a higher RMSF value, indicating reduced binding stability to the ligand, whereas the control compound displayed a lower RMSF value, suggesting enhanced binding stability. The residues at positions 880–920 and 1,025–1050 exhibited a reduced RMSF value. This region corresponds to the binding pocket, signifying the enhanced stability attributed to ligand interactions with the residues at this site. During the simulation, the SASA values for compounds 4, 8, and 11, and the control compound consistently differed from the remaining seven compounds, displaying lower values and a steadier trend, suggesting a more constrained conformation (Supplementary Figure SASA). Additionally, the SASA value, calculated based on protein composition, showed an enhanced stability trend for compounds 4 and 8 (refer to D and H in Supplementary Figure SASA). All 10 compounds exhibited lower total energy than the control compound (Supplementary Figure energy). The total energy fluctuations of compounds 6, 7, and 11 closely resembled those of the control compound (refer to F, G, and J in Supplementary Figure energy). In particular, compound 11 demonstrated a performance similar to that of axitinib in MD simulations, making it a promising VEGFR2 inhibitor.

While compounds 2, 4, 7, and 10 showed lower oral rat LD_{50} values, indicating higher toxicity compared to the estimated toxicity of axitinib, compounds 1, 3, 5, 6, 8, and 11 exhibited lower toxicity, as evidenced by the toxicity assessment results shown in Table 1. Notably, compound 11 demonstrated the lowest estimated toxicity. Moreover, the experimental data for compound 11 included in

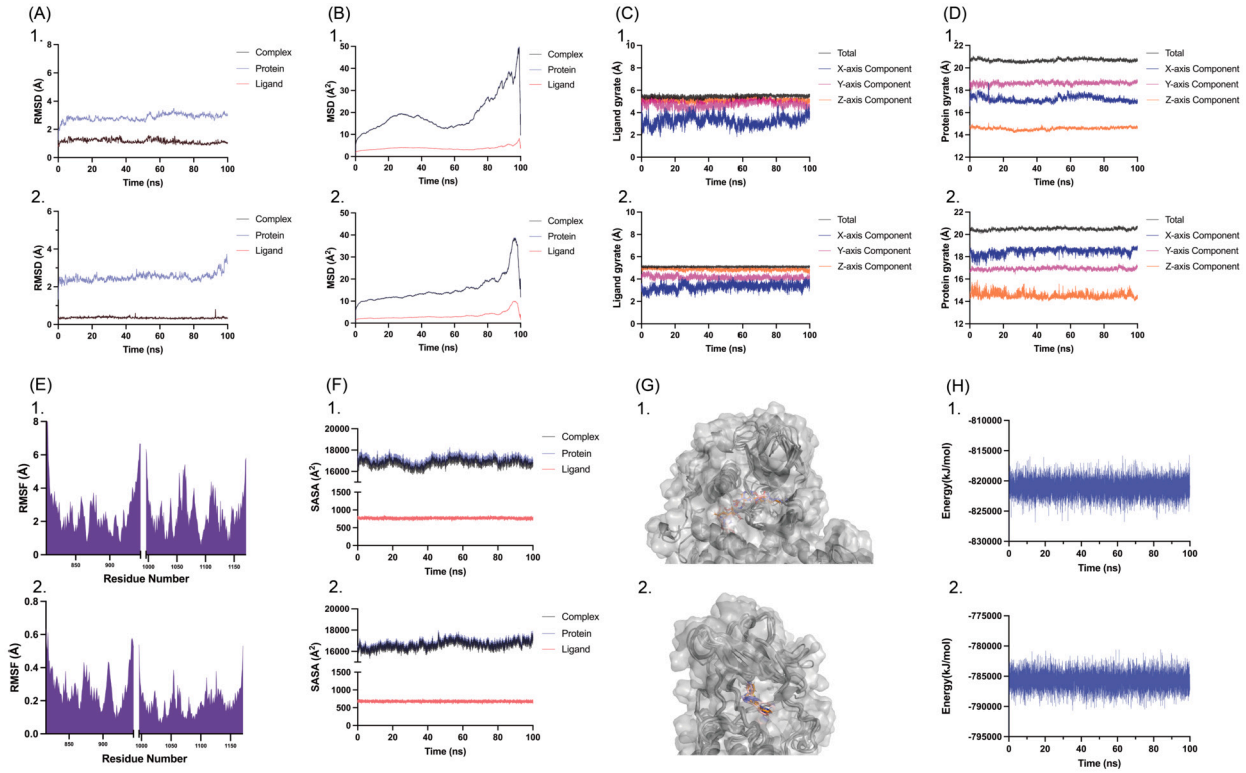

Fig. 7. (A) 1.: Root mean square deviation (RMSD) of the complex, VEGFR2 and the Compound 11. (A) 2.: RMSD of the complex, VEGFR2 and the AXI. (B) 1.: Mean square displacement (MSD) of the VEGFR2 and Compound 11 in the complex. (B) 2.: MSD of the VEGFR2 and AXI in the complex. (C) 1.: Gyrate of the Compound 11 in the complex. (C) 2.: Gyrate of the AXI in the complex. (D) 1.: Gyrate of the VEGFR2 in the compound 11 complex. (D) 2.: Gyrate of the VEGFR2 in the AXI complex. (E): Root mean square fluctuation (RMSF) of the VEGFR2 in the compound 11 complex and the AXI complex. (F) 1.: Solvent-accessible surface area (SASA) of the VEGFR2 and the Compound 11 in the complex. (F) 2.: SASA of the VEGFR2 and the AXI in the complex. (G) 1.: The Compound 11 complex structures at 0ns, cluster and 100ns. (G) 2.: The AXI complex structures at 0ns, cluster and 100ns. (H) The total energy of the Compound 11 complex and the AXI complex.

TEST revealed an oral rat LD_{50} value of 17011.96 mg/kg [57], further supporting its lower toxicity compared to the estimated toxicity of axitinib.

5. Conclusion

The outcomes of the Gyrate and SASA analyses in the comparative assessment of compound 11 and the control compound axitinib demonstrated substantial consistency. In contrast, axitinib exhibited a lower RMSF value and lower energy, indicative of higher stability in the binding interaction between the drug molecule axitinib and the receptor over the course of 100 ns. The structures at 0 ns, clusters, and 100 ns also visually reflected the more stable binding characteristics of axitinib to VEGFR2. Thus, compound 11 and the existing drug axitinib exhibit distinct advantages. Compound 11 emerged as a promising lead compound with the potential for subsequent drug development endeavors aimed at targeting VEGFR2.

One limitation of this study is the lack of experimental validation. Although promising, the proposed strategy may face challenges in translating the findings into clinical settings. In *vitro* and in *silico* predictions do not fully capture the dynamic and multifaceted nature of human physiology and pathology, potentially leading to discrepancies between predicted and actual outcomes in clinical trials. In the future, more robust experiments, including studies involving cell lines and animals, will be employed to further validate the compounds identified in this study. Nevertheless, the computational approach used in this study contributed significantly to cost reduction and time savings in the drug-design process. Another limitation of this study is that the results relied solely on the software MOE. Although MOE was chosen for its comprehensive suite of tools and proven accuracy in docking studies, future studies could benefit from integrating results obtained from multiple software platforms for docking studies. This approach would further enhance the reliability and justification of the screened compounds. Moreover, this study solely utilized the well-known axitinib as a benchmark drug to substantiate a proof-of-concept, demonstrating the viability of our methodology. In the future, further and more recent FDA-approved drugs aimed at targeting VEGFR2 will be assessed and compared in a follow-up study. Finally, potential adverse immune reactions that these compounds might induce were not considered at this stage. In the future, integrated in vitro and in vivo studies to evaluate the immunogenicity of the lead compounds will be crucial for understanding their potential in therapeutic applications.

Another potential direction for future research could involve integrating multi-omics data (genomics, transcriptomics, and proteomics) to enhance the predictive power of the models, thus providing a more comprehensive understanding of the molecular landscape associated with VEGFR2 inhibition and facilitating the identification of more precise drug candidates. Additionally, considering potential off-target effects, conducting molecular docking simulations in the future to predict the binding affinity of inhibitors to proteins other than VEGFR2, especially those with structures similar to VEGFR2, will aid in identifying potential off-target effects of the identified molecules. Furthermore, as drug stoichiometry analysis plays a critical role in drug discovery, integrating experiments with computational predictions in the future will facilitate further investigation into the effectiveness of protein binding.

In conclusion, this study introduced a novel approach using 3D deep learning and structural modeling for the design of potential VEGFR2 inhibitors. Employing a geometric-enhanced molecular representation learning method and flexible docking, this study identified candidate compounds with more favorable properties than the FDA-approved drug axitinib.

Data sharing statement

The data underlying this study are publicly available in BindingDB at https://www.bindingdb.org/ and ChEMBL21 at https://www.ebi.ac.uk/chembl/.

CRediT authorship contribution statement

Mengyang Xu: Writing – original draft, Methodology, Investigation, Formal analysis, Data curation, Conceptualization. **Xiaoyue Xiao:** Investigation, Formal analysis. **Yinglu Chen:** Investigation, Formal analysis. **Xiaoyan Zhou:** Writing – review & editing. **Luca Parisi:** Writing – review & editing, Supervision. **Renfei Ma:** Writing – review & editing, Supervision, Project administration, Funding acquisition, Conceptualization.

Declaration of competing interest

The authors declare that they have no known competing financial interests or personal relationships that could have appeared to influence the work reported in this paper.

Acknowledgements

This work was supported by the National Natural Science Foundation of China (grant no. 32300540) and the Science, Technology and Innovation Commission of Shenzhen Municipality (grant no. RCBS20221008093338092).

Appendix A. Supplementary material

Supplementary material related to this article can be found online at https://doi.org/10.1016/j.heliyon.2024.e35769.

References

[1] R.L. Siegel, K.D. Miller, A. Jemal, Cancer statistics, 2018, CA Cancer J. Clin. 68 (1) (2018) 7–30.
[2] B.S. Chhikara, K. Parang, Global cancer statistics 2022: the trends projection analysis, Chem. Biol. Lett. 10 (1) (2023) 451.
[3] S.M. Weis, D.A. Cheresh, Tumor angiogenesis: molecular pathways and therapeutic targets, Nat. Med. 17 (11) (2011) 1359–1370.
[4] J. Folkman, D. Hanahan, Switch to the angiogenic phenotype during tumorigenesis, in: Princess Takamatsu Symposia, vol. 22, 1991, pp. 339–347.
[5] J. Folkman, Tumor angiogenesis: therapeutic implications, N. Engl. J. Med. 285 (21) (1971) 1182–1186.
[6] A.S. Chung, J. Lee, N. Ferrara, Targeting the tumour vasculature: insights from physiological angiogenesis, Nat. Rev. Cancer 10 (7) (2010) 505–514.
[7] N. Ferrara, Vegf-a: a critical regulator of blood vessel growth, Eur. Cytokine Netw. 20 (4) (2009) 158–163.
[8] C. Huang, Y. Wang, J. Huang, H. Liu, Z. Chen, Y. Jiang, Y. Chen, F. Qian, A bioengineered anti-vegf protein with high affinity and high concentration for intravitreal treatment of wet age-related macular degeneration, Bioeng. Transl. Med. 10632 (2023).
[9] P. Carmeliet, Vegf as a key mediator of angiogenesis in cancer, Oncology 69 (Suppl. 3) (2005) 4–10.
[10] Z.K. Otrock, J.A. Makarem, A.I. Shamseddine, Vascular endothelial growth factor family of ligands and receptors, Blood Cells Mol. Dis. 38 (3) (2007) 258–268.
[11] S. Rampogu, A. Baek, C. Park, M. Son, S. Parate, S. Parameswaran, Y. Park, B. Shaik, J.H. Kim, S.J. Park, et al., Discovery of small molecules that target vascular endothelial growth factor receptor-2 signalling pathway employing molecular modelling studies, Cells 8 (3) (2019) 269.
[12] P. Carmeliet, R.K. Jain, Molecular mechanisms and clinical applications of angiogenesis, Nature 473 (7347) (2011) 298–307.
[13] N. Ferrara, H.-P. Gerber, J. LeCouter, The biology of vegf and its receptors, Nat. Med. 9 (6) (2003) 669–676.
[14] R.J. Motzer, T.E. Hutson, D. Cella, J. Reeves, R. Hawkins, J. Guo, P. Nathan, M. Staehler, P. Souza, J.R. Merchan, et al., Pazopanib versus sunitinib in metastatic renal-cell carcinoma, N. Engl. J. Med. 369 (8) (2013) 722–731.
[15] M. Kudo, K. Motomura, Y. Wada, Y. Inaba, Y. Sakamoto, M. Kurosaki, Y. Umeyama, Y. Kamei, J. Yoshimitsu, Y. Fujii, et al., Avelumab in combination with axitinib as first-line treatment in patients with advanced hepatocellular carcinoma: results from the phase 1b vegf liver 100 trial, Liver Cancer 10 (3) (2021) 249–259.
[16] L. Huang, L. Fu, Mechanisms of resistance to egfr tyrosine kinase inhibitors, Acta Pharm. Sin. B 5 (5) (2015) 390–401.
[17] O. Leiva, I. Bohart, T. Ahuja, D. Park, Off-target effects of cancer therapy on development of therapy-induced arrhythmia: a review, Cardiology (2023).
[18] J.M. Bowen, Mechanisms of tki-induced diarrhea in cancer patients, Curr. Opin. Support. Palliat. Care 7 (2) (2013) 162–167.
[19] V. Grünwald, M.H. Voss, B.I. Rini, T. Powles, L. Albiges, R.H. Giles, E. Jonasch, Axitinib plus immune checkpoint inhibitor: evidence- and expert-based consensus recommendation for treatment optimisation and management of related adverse events, Br. J. Cancer 123 (6) (2020) 898–904.
[20] K.E. Arnst, S. Banerjee, H. Chen, S. Deng, D.-J. Hwang, W. Li, D.D. Miller, Current advances of tubulin inhibitors as dual acting small molecules for cancer therapy, Med. Res. Rev. 39 (4) (2019) 1398–1426.

[21] A. Anighoro, J. Bajorath, G. Rastelli, Polypharmacology: challenges and opportunities in drug discovery: miniperspective, J. Med. Chem. 57 (19) (2014) 7874–7887.
[22] J.P. Hughes, S. Rees, S.B. Kalindjian, K.L. Philpott, Principles of early drug discovery, Br. J. Pharmacol. 162 (6) (2011) 1239–1249.
[23] Z. Chen, X. Wang, X. Chen, J. Huang, C. Wang, J. Wang, Z. Wang, Accelerating therapeutic protein design with computational approaches toward the clinical stage, Comput. Struct. Biotechnol. J. (2023).
[24] A. Leaver-Fay, M. Tyka, S.M. Lewis, O.F. Lange, J. Thompson, R. Jacak, K.W. Kaufman, P.D. Renfrew, C.A. Smith, W. Sheffler, et al., Rosetta3: an object-oriented software suite for the simulation and design of macromolecules, in: Methods in Enzymology, vol. 487, Elsevier, 2011, pp. 545–574.
[25] Z. Zhu, Z. Yao, G. Qi, N. Mazur, P. Yang, B. Cong, Associative learning mechanism for drug-target interaction prediction, CAAI Trans. Intell. Technol. 8 (4) (2023) 1558–1577.
[26] Z. Zhu, Z. Yao, X. Zheng, G. Qi, Y. Li, N. Mazur, X. Gao, Y. Gong, B. Cong, Drug–target affinity prediction method based on multi-scale information interaction and graph optimization, Comput. Biol. Med. 167 (2023) 107621.
[27] A. Ajmal, M. Danial, M. Zulfat, M. Numan, S. Zakir, C. Hayat, K.F. Alabbosh, M.E. Zaki, A. Ali, D. Wei, In silico prediction of new inhibitors for kirsten rat sarcoma g12d cancer drug target using machine learning-based virtual screening, molecular docking, and molecular dynamic simulation approaches, Pharmaceuticals 17 (5) (2024) 551.
[28] R.E. Amaro, A.J. Mulholland, Multiscale methods in drug design bridge chemical and biological complexity in the search for cures, Nat. Rev. Chem. 2 (4) (2018) 0148.
[29] M. Karplus, Development of multiscale models for complex chemical systems: from h+ h 2 to biomolecules (Nobel lecture), Angew. Chem. 38 (53) (2014) 9992–10005.
[30] M. Honma, H. Suzuki, Can molecular dynamics facilitate the design of protein–protein-interaction inhibitors?, Nat. Rev. Rheumatol. 19 (1) (2023) 8–9.
[31] B.J. Bender, S. Gahbauer, A. Luttens, J. Lyu, C.M. Webb, R.M. Stein, E.A. Fink, T.E. Balius, J. Carlsson, J.J. Irwin, et al., A practical guide to large-scale docking, Nat. Protoc. 16 (10) (2021) 4799–4832.
[32] R. Gupta, D. Srivastava, M. Sahu, S. Tiwari, R.K. Ambasta, P. Kumar, Artificial intelligence to deep learning: machine intelligence approach for drug discovery, Mol. Divers. 25 (2021) 1315–1360.
[33] X. Wang, K. Song, L. Li, L. Chen, Structure-based drug design strategies and challenges, Curr. Top. Med. Chem. 18 (12) (2018) 998–1006.
[34] X. Fang, L. Liu, J. Lei, D. He, S. Zhang, J. Zhou, F. Wang, H. Wu, H. Wang, Geometry-enhanced molecular representation learning for property prediction, Nat. Mach. Intell. 4 (2) (2022) 127–134.
[35] F. Sangande, E. Julianti, D.H. Tjahjono, Ligand-based pharmacophore modeling, molecular docking, and molecular dynamic studies of dual tyrosine kinase inhibitor of egfr and vegfr2, Int. J. Mol. Sci. 21 (20) (2020) 7779.
[36] N.K. Velayutham, T. Thamaraikani, S. Wahab, M. Khalid, G. Ramachawolran, S.S. Abullais, L.S. Wong, M. Sekar, S.H. Gan, A.J. Ebenezer, et al., Stylopine: a potential natural metabolite to block vascular endothelial growth factor receptor 2 (vegfr2) in osteosarcoma therapy, Front. Pharmacol. 14 (2023) 1150270.
[37] M.K. Gilson, T. Liu, M. Baitaluk, G. Nicola, L. Hwang, J. Chong, Bindingdb in 2015: a public database for medicinal chemistry, computational chemistry and systems pharmacology, Nucleic Acids Res. 44 (D1) (2016) 1045–1053.
[38] B. Zdrazil, E. Felix, F. Hunter, E.J. Manners, J. Blackshaw, S. Corbett, M. Veij, H. Ioannidis, D.M. Lopez, J.F. Mosquera, et al., The chembl database in 2023: a drug discovery platform spanning multiple bioactivity data types and time periods, Nucleic Acids Res. 52 (D1) (2024) 1180–1192.
[39] C. Knox, M. Wilson, C.M. Klinger, M. Franklin, E. Oler, A. Wilson, A. Pon, J. Cox, N.E. Chin, S.A. Strawbridge, et al., Drugbank 6.0: the drugbank knowledgebase for 2024, Nucleic Acids Res. 52 (D1) (2024) 1265–1275.
[40] S. Kim, J. Chen, T. Cheng, A. Gindulyte, J. He, S. He, Q. Li, B.A. Shoemaker, P.A. Thiessen, B. Yu, et al., Pubchem 2023 update, Nucleic Acids Res. 51 (D1) (2023) 1373–1380.
[41] M.A. McTigue, J.A. Wickersham, C. Pinko, R.E. Showalter, C.V. Parast, A. Tempczyk-Russell, M.R. Gehring, B. Mroczkowski, C.-C. Kan, J.E. Villafranca, et al., Crystal structure of the kinase domain of human vascular endothelial growth factor receptor 2: a key enzyme in angiogenesis, Structure 7 (3) (1999) 319–330.
[42] H.A. Zhong, S. Almahmoud, Docking and selectivity studies of covalently bound janus kinase 3 inhibitors, Int. J. Mol. Sci. 24 (7) (2023) 6023.
[43] D. Jiang, Z. Wu, C.-Y. Hsieh, G. Chen, B. Liao, Z. Wang, C. Shen, D. Cao, J. Wu, T. Hou, Could graph neural networks learn better molecular representation for drug discovery? A comparison study of descriptor-based and graph-based models, J. Cheminform. 13 (1) (2021) 1–23.
[44] Z. Guo, K. Guo, B. Nan, Y. Tian, R.G. Iyer, Y. Ma, O. Wiest, X. Zhang, W. Wang, C. Zhang, et al., Graph-based molecular representation learning, arXiv preprint, arXiv:2207.04869, 2022.
[45] X. Chen, Z. Chen, D. Xu, Y. Lyu, Y. Li, S. Li, J. Wang, Z. Wang, De novo design of g protein-coupled receptor 40 peptide agonists for type 2 diabetes mellitus based on artificial intelligence and site-directed mutagenesis, Front. Bioeng. Biotechnol. 9 (2021) 694100.
[46] C.R. Corbeil, C.I. Williams, P. Labute, Variability in docking success rates due to dataset preparation, J. Comput.-Aided Mol. Des. 26 (6) (2012) 775–786.
[47] M.J. Abraham, T. Murtola, R. Schulz, S. Páll, J.C. Smith, B. Hess, E. Lindahl, Gromacs: high performance molecular simulations through multi-level parallelism from laptops to supercomputers, SoftwareX 1 (2015) 19–25.
[48] V. Zoete, M.A. Cuendet, A. Grosdidier, O. Michielin, Swissparam: a fast force field generation tool for small organic molecules, J. Comput. Chem. 32 (11) (2011) 2359–2368.
[49] N. Bou-Rabee, A. Donev, E. Vanden-Eijnden, Metropolis integration schemes for self-adjoint diffusions, Multiscale Model. Simul. 12 (2) (2014) 781–831.
[50] R. Martoňák, A. Laio, M. Parrinello, Predicting crystal structures: the Parrinello-Rahman method revisited, Phys. Rev. Lett. 90 (7) (2003) 075503.
[51] J. Huang, S. Rauscher, G. Nawrocki, T. Ran, M. Feig, B.L. Groot, H. Grubmüller, A.D. MacKerell, Charmm36: an improved force field for folded and intrinsically disordered proteins, Biophys. J. 112 (3) (2017) 175–176.
[52] Z.-D. Chen, L. Zhao, H.-Y. Chen, J.-N. Gong, X. Chen, C.Y.-C. Chen, A novel artificial intelligence protocol to investigate potential leads for Parkinson's disease, RSC Adv. 10 (39) (2020) 22939–22958.
[53] Z. Wang, H. Sun, X. Yao, D. Li, L. Xu, Y. Li, S. Tian, T. Hou, Comprehensive evaluation of ten docking programs on a diverse set of protein–ligand complexes: the prediction accuracy of sampling power and scoring power, Phys. Chem. Chem. Phys. 18 (18) (2016) 12964–12975.
[54] X. Du, Y. Li, Y.-L. Xia, S.-M. Ai, J. Liang, P. Sang, X.-L. Ji, S.-Q. Liu, Insights into protein–ligand interactions: mechanisms, models, and methods, Int. J. Mol. Sci. 17 (2) (2016) 144.
[55] K. Patel, L.J. Walport, J.L. Walshe, P.D. Solomon, J.K. Low, D.H. Tran, K.S. Mouradian, A.P. Silva, L. Wilkinson-White, A. Norman, et al., Cyclic peptides can engage a single binding pocket through highly divergent modes, Proc. Natl. Acad. Sci. 117 (43) (2020) 26728–26738.
[56] A. Karasawa, T. Kawate, Structural basis for subtype-specific inhibition of the p2x7 receptor, eLife 5 (2016) 22153.
[57] CCTE, EPA: the United States environmental protection agency's center for computational toxicology and exposure, https://doi.org/10.23645/epacomptox.21379365.v3.
[58] M.H. Abdurahman, A.Z. Abdullah, W. Da Oh, N.F. Shopware, M.F. Gasim, P. Okoye, A. Ul-Hamid, A.R. Mohamed, Tunable band structure of synthesized carbon dots modified graphitic carbon nitride/bismuth oxychlorobromide heterojunction for photocatalytic degradation of tetracycline in water, J. Colloid Interface Sci. 629 (2023) 189–205.
[59] M. Cai, Y. Liu, K. Dong, C. Wang, S. Li, A novel s-scheme heterojunction of cd0. 5zn0. 5s/biocl with oxygen defects for antibiotic norfloxacin photodegradation: performance, mechanism, and intermediates toxicity evaluation, J. Colloid Interface Sci. 629 (2023) 276–286.
[60] Y. Liu, S. Liu, M. Chen, Y. Bai, Y. Liu, J. Mei, B. Lai, Enhanced tc degradation by persulfate activation with carbon-coated cufe2o4: the radical and non-radical co-dominant mechanism, dft calculations and toxicity evaluation, J. Hazard. Mater. 461 (2024) 132417.